J. Fluid Mech. (2013), *vol.* 729, *pp.* 377–387.
doi:10.1017/jfm.2013.295

Topology-induced effect in biomimetic propulsive wakes

V. Raspa†, R. Godoy-Diana and B. Thiria

Physique et Mécanique des Milieux Hétérogènes (PMMH), CNRS UMR7636; ESPCI ParisTech; UPMC (Paris 6); Univ. Paris Diderot (Paris 7), 10, rue Vauquelin, F-75005 Paris, France

(Received 8 February 2013; revised 30 May 2013; accepted 5 June 2013)

It is known that the wake pattern observed in a cross-section behind swimming or flying animals is typically characterized by the presence of periodical vortex shedding. However, depending on species, propulsive wakes can differ according to the spatial ordering of the main vortex structures. We conducted a very precise experiment to analyse the role of the topology of the wake in the generation of propulsion by comparing two prototypical cases in a quasi-two-dimensional view. One configuration is jellyfish-like, with symmetric shedding of vortex pairs, and the other is fish-like, with alternating shedding of counter-rotating vortices. Self-propulsion is achieved by the flapping motion of two identical pitching rigid foils, separated by a distance d. By keeping the momentum input unchanged, we compared both symmetric and asymmetric flapping modes. For the entire explored range of parameters, the symmetric jellyfish-like mode has shown to produce more thrust than the fish-like asymmetrical one. We show here that this difference is due to a pressure effect related to the ability of each wake to produce or not, strong fluctuations of transversal velocities in the near-wake region.

Key words: swimming/flying, vortex streets, wakes/jets

1. Introduction

Locomotive animal–fluid interactions in the macroscopic scale, such as those birds and fish have with their natural environments, typically occur in the Reynolds number regime of $Re \geqslant 10^2$. This is the *Eulerian regime* (Childress 1981), where the resulting complex flow field is characterized by the formation and periodical shedding of vortices (Lighthill 1960; Saffman 1992). It is the case for wakes observed behind the flapping wings of a bird (Hedenström, Rosén & Spedding 2006), a fish tail (Fish & Lauder 2006) or other swimming appendages such as for squid or salps (Sutherland & Madin 2010). Depending on the species, propulsive wakes are distinguished by the spatial ordering of their vortex pattern. A main classification can be established by observing a cross-section of the wake, where the series of counter-rotating vortices can be arranged either symmetrically (vortex ring configuration) or asymmetrically (staggered vortex street configuration). From the abundant examples found in the

† Email address for correspondence: veronica.raspa@espci.fr

literature, symmetrical wakes are produced by squid (Anderson & Grosenbaugh 2005) or jellyfish (Dabiri *et al.* 2005), whereas asymmetrical or staggered wakes are produced by swimming fish, eels or watersnakes (Müller *et al.* 1997).

The way hydrodynamics forces are linked to wake patterns has long been a central question for physicists and engineers. One of the major concerns, for instance, is in drag reduction in the design of cars (Katz 2006) and aircraft (Joslin 1998; Spalart & McLean 2011) where the presence of a wake and its proper structure is known to play a major role for the friction laws. Following the same line of thought, the problem of dynamic stalls of flying and swimming objects is thus worth investigation, especially for the purposes of biomechanics (Ellington *et al.* 1996; Birch, Dickson & Dickinson 2004). Basically, shed structures created during stroke cycles transport the momentum of displaced fluid by the wings or tail that enable the animal to move. In that case, no specific spatial arrangement is directly involved in the mechanism of thrust force production.

However, a more thorough analysis shows that the way vorticity is distributed in the wake (i.e. the spatiotemporal characteristics of the velocity field) can have a major influence on the effective propulsion. For instance, it has been shown (Krueger 2005; Ruiz, Whittlesey & Dabiri 2011) that vortex ring propulsion could be more efficient than its straight jet equivalent (i.e. starting from the same momentum input). On the other hand, for staggered shedding, the strict consideration of momentum can lead to a large overestimation of the mean force for strongly fluctuating velocity fields (Bohl & Koochesfahani 2009). The effect of shed structures on thrust generation, was recently investigated using artificial wakes (Raspa, Gaubert & Thiria 2012). The authors brought the main conclusion that symmetric wake geometries were more efficient than the asymmetric ones, based on their ability of generating strong fluctuations on transversal velocities or not. However, the authors were considering a constant momentum injection provided by a still object, therefore far from a self-propelled flapping animal.

The goal of the present paper is to quantify, for real self-propelled moving objects, how thrust production can be affected by the wake characteristics (i.e. spatial ordering, intensity of the velocity fluctuations) while the momentum available for thrust production is kept constant. The self-propelled swimmer of the present experiment does not aim at mimicking a real fish or bird. However, it develops controlled periodical vortex shedding to the wake, sharing physical key mechanisms for propulsion with real animals. The main idea is to extract optimal design strategies from the locomotive mechanisms developed by nature in order to transpose them to technological applications. Indeed, we show in this paper that controlling velocity fluctuations in the near wake can increase significantly thrust production for a given momentum input, a result that can be valuable in the design and optimization of artificial biomimetic propellers.

2. The experimental device

The experiment was performed in a free-surface water tank (900 mm $\times$ 800 mm $\times$ 500 mm) where an artificial swimmer is submerged. Self-propulsion is achieved by the pitching motion of two rigid foils such as that used in Godoy-Diana, Aider & Wesfreid (2008). The foils are separated by a distance d; the chord (c), maximum width (D) and span (l) are 24 mm, 5 mm and 100 mm, respectively. The angular position of each flap is controlled with 0.5° of precision, by a small stepper and an adequate driving curve. The set was placed in a cart hanging from a straight

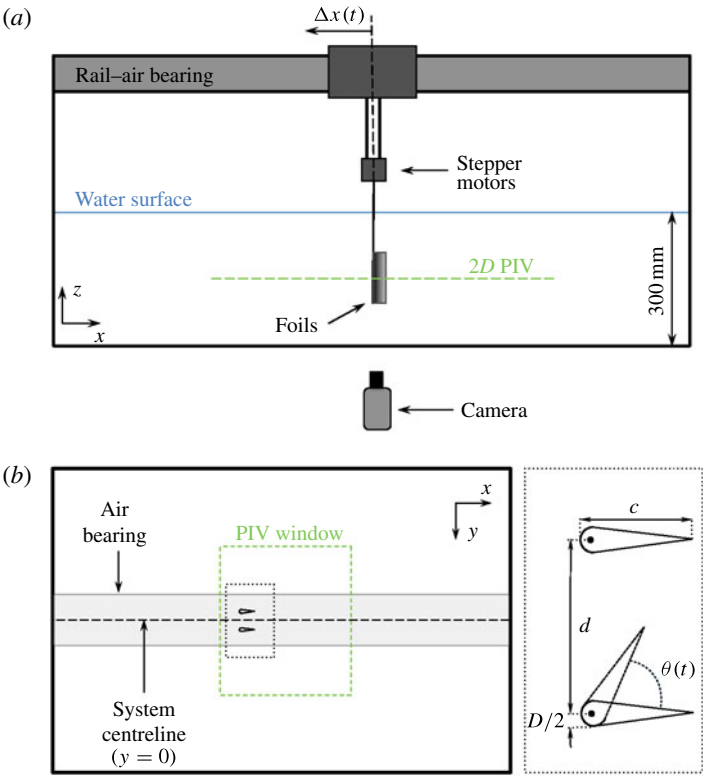

FIGURE 1. (Colour online) Sketches of the experimental device. (*a*) Side view presenting the general assembling. (*b*) The camera view showing details on the foil configuration and the definition of the geometrical parameters.

rail, allowing it to glide along the longitudinal direction. In order to minimize the friction, an air bearing was used. Sketches of the experimental set-up are presented in figure 1(*a,b*).

We considered two different flapping configurations for self-propelled swimming, which we have named *symmetrical* (*S*) and *asymmetrical* (*A*) after the kind of pattern of the resulting wake. The first case is illustrated on the left in figure 2(*a*): both flaps pitch towards each other in phase, producing counter-rotating pairs of vortices that are simultaneously shed into the wake. On the left, the second case is exemplified. A phase lag ($\Delta\phi$) is introduced between the pitching motion of the two flaps so that, although each flap independently follows the same motion profile as in the symmetrical configuration, the resulting wake is no longer symmetric and bears more resemblance to a fish-like wake (see online movies ESM1 and ESM2 available at http://dx.doi.org/10.1017/jfm.2013.295). The insets in figure 2(*b*) illustrate the driving curves used to control the angular position of the flaps, $\theta(t/\tau)$, for both considered flapping configurations. Time derivatives were tuned in order to minimize vorticity ejection during the expansion phase of the flaps' oscillation. The example corresponds to an amplitude θ_{max} of 60°. The initial value ($\theta = 0$) of the angular excursion was set aligning the flaps with the *x*-direction. It is worth noting that all of the driving curves in figure 2(*b*) are essentially the same, the phase lag being the only difference. Therefore, the momentum input for both flapping configurations is also the same.

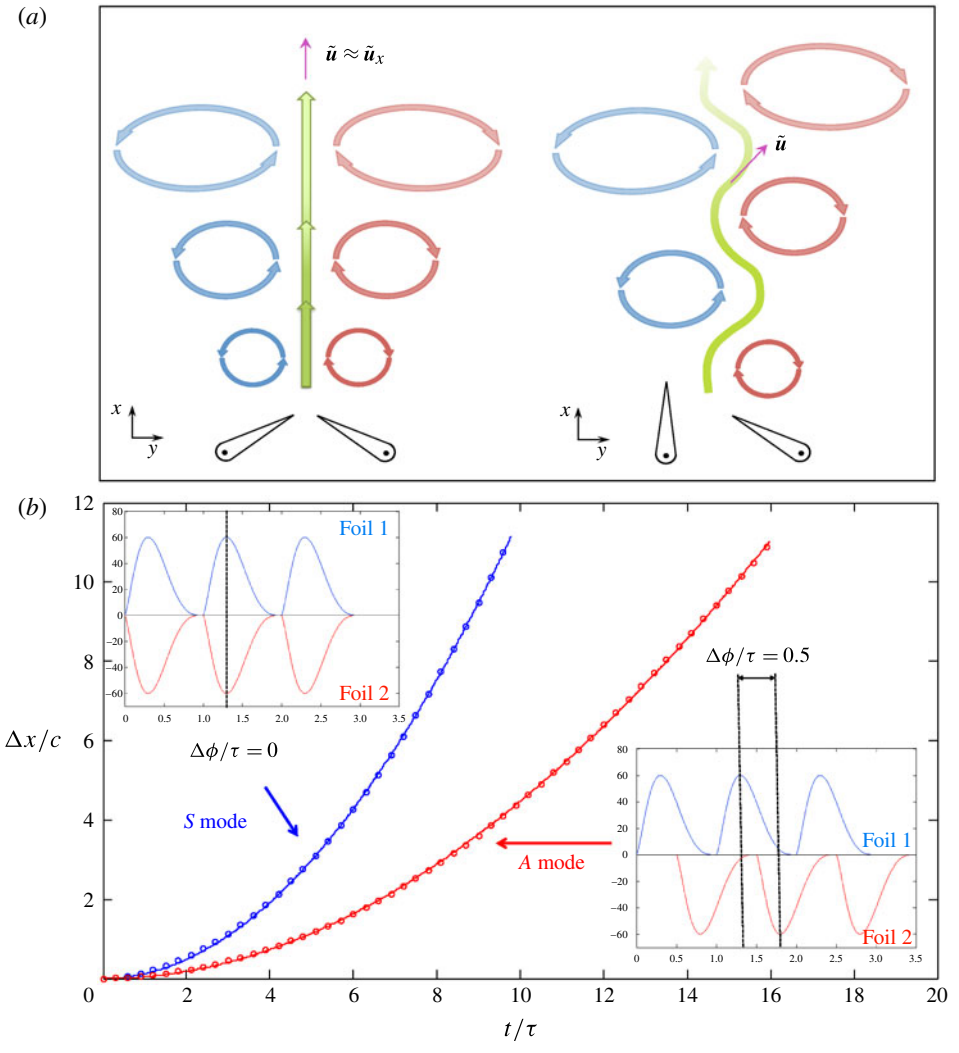

FIGURE 2. (Colour online) (*a*) Simplified schemes illustrating the topology and velocity fluctuations ($\tilde{\boldsymbol{u}}$) of the considered wakes. Left: *S* mode, resembling thrust wakes such as behind jellyfish. Counter-rotating pairs of vortices are simultaneously shed into the wake. Right: *A* mode, similar to thrust wakes such as behind flapping wings or tails. Counter-rotating vortices are alternatively shed into the wake by the flapping motion. (*b*) Swimmer's reduced displacement ($\Delta x/c$) measured for a flapping frequency of 5 Hz and $d/c = 1.47$; on both flapping configurations. Measurements were fitted with (2.2) (full lines). Substantially different displacements are achieved from the same momentum input. Driving curves are correspondingly shown; all profiles are essentially the same, the phase lag ($\Delta\phi$) being the only difference.

Asymmetrical wakes are usually created by a single foil, however, we used here two pitching foils to create both wakes in order to compare thrust production achieved from the same input. If all of the other experimental parameters remain unchanged, the phase lag between the angular positions of the two flaps controls the symmetry of the resulting thrust wake. Of course, the efficiency of the swimmer should integrate the

knowledge of the torque produced by the motors. Unfortunately, our step motors are unable to give the torque, this is the purpose of a forthcoming paper.

As mentioned above, the pitching motion of the flaps determines the system to be self-propelled. The reduced displacement, $\Delta x/c$, of our artificial swimmer was measured as a function of time on both flapping configurations for frequencies ranging from 2 to 5 Hz, setting d between $1.47c$ and $10c$, and $\theta_{max} = 60°$. Measurements show that after a clear transitory, the swimmer reaches constant velocity. Even though the momentum input is the same on both configurations, the outcome displacement is significantly different. Figure 2(*b*) exemplifies the measurements for a frequency of 5 Hz and $d/c = 1.47$.

The propulsive force was recovered from the swimmer displacement measurements, such as those presented in figure 2(*b*). The swimmer position was recovered from imaging processing with 2 mm of accuracy. The following dynamical model was proposed to describe the measurements:

$$m\ddot{x} + \gamma \dot{x}^2 = F_p^{S,A} \tag{2.1}$$

where $m = 2.8$ kg is the total mass of the swimmer, $\gamma \dot{x}^2$ is the nonlinear hydrodynamic drag term and $F_p^{S,A}$ is the effective propulsive force. Both $F_p^{S,A}$ and γ are independent unknown coefficients to be determined from the measurements. The superscript (S or A), refers to the symmetry of the corresponding flapping mode. Time derivatives are indicated with dots over the variable. For the sake of clarity, the explicit time dependence of the displacement x was ignored in (2.1). Considering as initial conditions that $x(0) = 0$ and $\dot{x}(0) = 0$, (2.1) gives

$$x(t) = \frac{m}{\gamma} \log \left[\cosh \frac{\sqrt{\gamma F_p^{S,A}}}{m} t \right]. \tag{2.2}$$

To estimate the propulsive force, measurements were fitted with (2.2). An example of the data fitting is presented in solid lines on figure 2(*b*). A Monte Carlo scheme was used to propagate the displacement uncertainty to the corresponding force and velocity measurements.

Fast two-dimensional particle image velocimetry (PIV) measurements were conducted on a fixed observation window to obtain the velocity field (typical sequences of vorticity field are shown as supplementary material, see online videos ESM3 and ESM4). The air bearing set-up was blocked on a fixed position for this purpose. Mean flow velocities and fluctuations, $\langle \boldsymbol{u} \rangle$ and $\tilde{\boldsymbol{u}}$, were extracted from them. The set-up was chosen for measurements consistency, considering that the swimming transient is needed for data fitting, the stationary state is very short in the accessible range and reached in the last part of the trajectory (see figure 2*b*). Instantaneous velocity fields generated during tethered and forward swimming could be different; nevertheless, our results (see figure 4) show that if there is any difference, it is not dramatically changing the mean flow velocities and/or the fluctuations. For a discussion on how to consider this potential difference see Ramananarivo, Godoy-Diana & Thiria (2011). PIV measurements were performed from pairs of images sequentially acquired with a Phantom v9.1 high-speed camera at full resolution of 1632×1200 pixels, controlled by LaVision DaVis 7.2 software. For that purpose, the record length, the inter-frame time and the record frequency were set to 10 s, 1.2 ms and 150 Hz, respectively. Polyethylene particles of 10 μm diameter were used for seeding and a 1 mm thick laser sheet placed at mid-span of the foils was produced

with a Quantronix Darwin-Duo 20 mJ pulsed laser. PIV calculations were performed with DaVis 7.2, using 16 pixels × 16 pixels interrogation windows with 50 % of overlap, giving a final density of 0.75 vectors mm^{-1}. Standard particle/laser sheet visualizations were made using 50 μm diameter polyethylene seeding particles. The two-dimensional approximation is reasonable in the near wake due to the coherence of the forcing along the span (see Poncet (2002) or Thiria, Goujon-Durand & Wesfreid (2006)).

3. Results and discussion

3.1. *Swimming performance*

Measurements as in figure 2(*b*) show that after a clear transitory, the swimmer reaches constant velocity (U_o). Figure 3(*a*) presents the comparison between the velocities achieved by both flapping configurations, calculated from the corresponding displacement measurements. While the symmetric mode proved to be the fastest for a short axis separation, no significant difference between the configurations was detected on the swimming performance if the flaps are separated enough. A similar observation, but on thrust production, can be made from figure 3(*d*) where the ratio F_p^S/F_p^A is plotted as a function of d/c for different flapping frequencies. As long as the flaps are not placed too close to each other, the performance of both flapping modes as thrust generators is approximately the same. An average difference between thrust achieved by each configuration, $\Delta_o = (2.4 \pm 0.3)$ mN, was estimated from the measurements. However, when the flaps separation distance is short enough, the symmetric mode has proved to generate higher thrust than the asymmetric one. The magnitudes of the forces F_p^S and F_p^A are shown in figure 3(*b,c*). The higher the flapping frequency, the greater the performance difference (see figure 4).

Since the momentum input remains unchanged, the self-propulsive swimming performance only depends on the wake topology given by the spatial ordering of the counter-rotating vortices periodically shed into the wake by the flapping motion. The following discussion on the role of symmetry in the generation of propulsion will be focused on the case of $d/c = 1.47$.

3.2. *Velocity field analysis*

The propulsive reaction force experienced by the swimmer can be deduced from a classic momentum balance on a given control volume. Considering average quantities and dropping the viscosity effects (negligible for inertial propulsion), the average propulsive force $\boldsymbol{F_p}$ is expressed as a simple contribution from the momentum $\rho\,\langle \boldsymbol{u}\rangle$ and the pressure $\langle p\rangle$ (Batchelor 1967; Spedding & Hedenström 2009):

$$\boldsymbol{F_p} = -\int_{S_e} \rho\,\langle \boldsymbol{u}\rangle\,\langle \boldsymbol{u}\rangle \cdot \boldsymbol{n}\,\mathrm{d}S - \int_{S_e} \langle p\rangle\,\boldsymbol{n}\,\mathrm{d}S. \tag{3.1}$$

where S_e is the boundary surface of the control volume, oriented by its external normal $\boldsymbol{n}$.

The average propulsive force per unit span was obtained from (3.1), for each considered case. To evaluate the first integral on the right term, mean flow velocities were correspondingly recovered from PIV measurements. Figure 5(*a,b*) exemplify the obtained mean axial velocities $\langle u_x\rangle$ for a flapping frequency of 5 Hz. The corresponding fluctuations $\langle \tilde{u}_x\rangle$ are presented in figure 5(*c,d*). Velocity fluctuations were calculated as the standard deviation of the corresponding average. In the same figure, the flaps are illustrated in white. Integrals were calculated at $1.8c$ from the

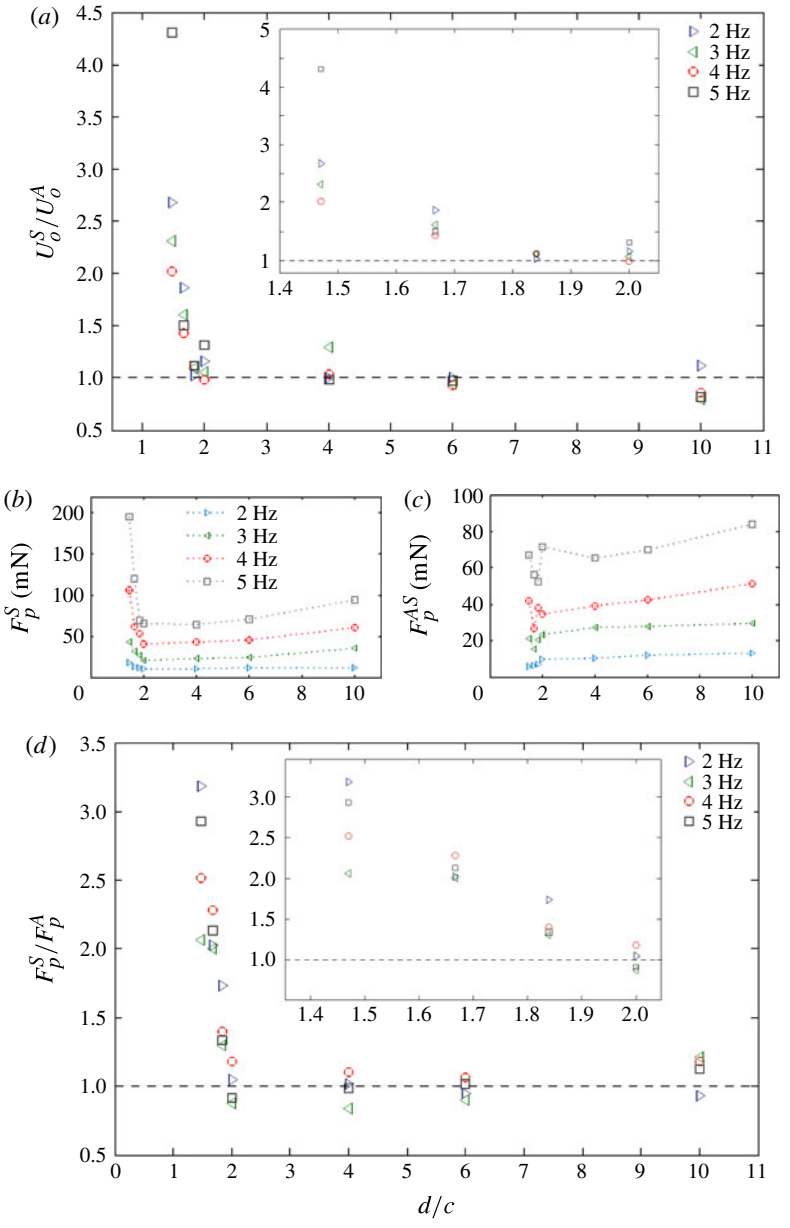

FIGURE 3. (Colour online) (*a*) Characteristic velocity ratio U_o^S/U_o^A as a function of d/c, comparing the swimming performance of both configurations. Velocity uncertainties are typically in the range of 5–10 %. (*b*,*c*) Magnitudes of the measured forces F_p^S and F_p^A, respectively. (*d*) Plot of F_p^S/F_p^A as a function of d/c for different flapping frequencies, comparing both flapping modes as thrust generators. Insets in (*a*,*d*) are magnifications of the 1.4–2 d/c range.

vertical position of the flap's tips at $t = 0$ (i.e. over the white dashed line at $x/c = 0$). A sensitivity analysis was performed by varying the position of the downstream boundary of the control volume between $x/c = 0$ and 2 to evaluate integrals in (3.1),

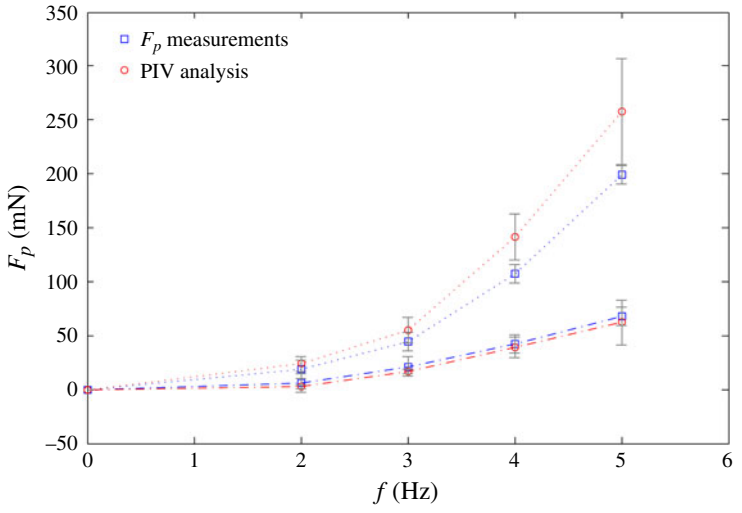

FIGURE 4. (Colour online) Squares (shown in blue online) show the propulsion achieved by both kinds of propellers, plotted together as a function of f, setting $d/c = 1.47$. Dashed-dot lines correspond to measurements made in the asymmetrical configuration, dotted lines indicate the symmetrical mode. The corresponding calculations, made from (3.1), are presented in as circles (shown in red online); see the text in § 3.2. For PIV force estimations, error bars were calculated as the standard deviation of values obtained after varying the position of the downstream boundary of the control volume within the region where viscous dissipation and/or three-dimensional effects are negligible.

ensuring that force estimations vary less than 15 % from the corresponding mean value. This range was defined to restrict the analysis to a region where viscous dissipation and/or three-dimensional effects could be reasonably neglected. The asymmetric flow appears here strongly decelerated, showing a much larger spreading angle than the symmetric flow (see the discussion in Raspa *et al.* (2012)). The latter, in contrast, is characterized by a strong propulsive jet in the axial direction and poor lateral fluctuations.

To complete the calculation of the propulsive force from (3.1), the mean pressure field is required. Equations for the evolution of mean flow variables to describe the underling turbulent flow, can be derived from the time-averaged Navier–Stokes equations and the Reynolds decomposition for the velocity and pressure fields (Pope 2000). For an inviscid incompressible two-dimensional fluid of uniform density ρ, the following mean-momentum equations are obtained (see also van Oudheusden *et al.* (2007) and Bohl & Koochesfahani (2009)):

$$\langle \boldsymbol{u} \rangle \cdot \boldsymbol{\nabla} \langle u_j \rangle = -\frac{\partial \langle \tilde{u}_j \tilde{u}_i \rangle}{\partial x_i} - \frac{1}{\rho} \frac{\partial \langle p \rangle}{\partial x_j} \tag{3.2}$$

where the subscripts i, j refer to the in-plane (x, y) coordinates. Within the context of the turbulent boundary layer approximation for developing jets Pope (2000) the lateral momentum equation becomes

$$\frac{1}{\rho} \frac{\partial \langle p \rangle}{\partial y} + \frac{\partial \langle \tilde{u}_y^2 \rangle}{\partial y} = 0. \tag{3.3}$$

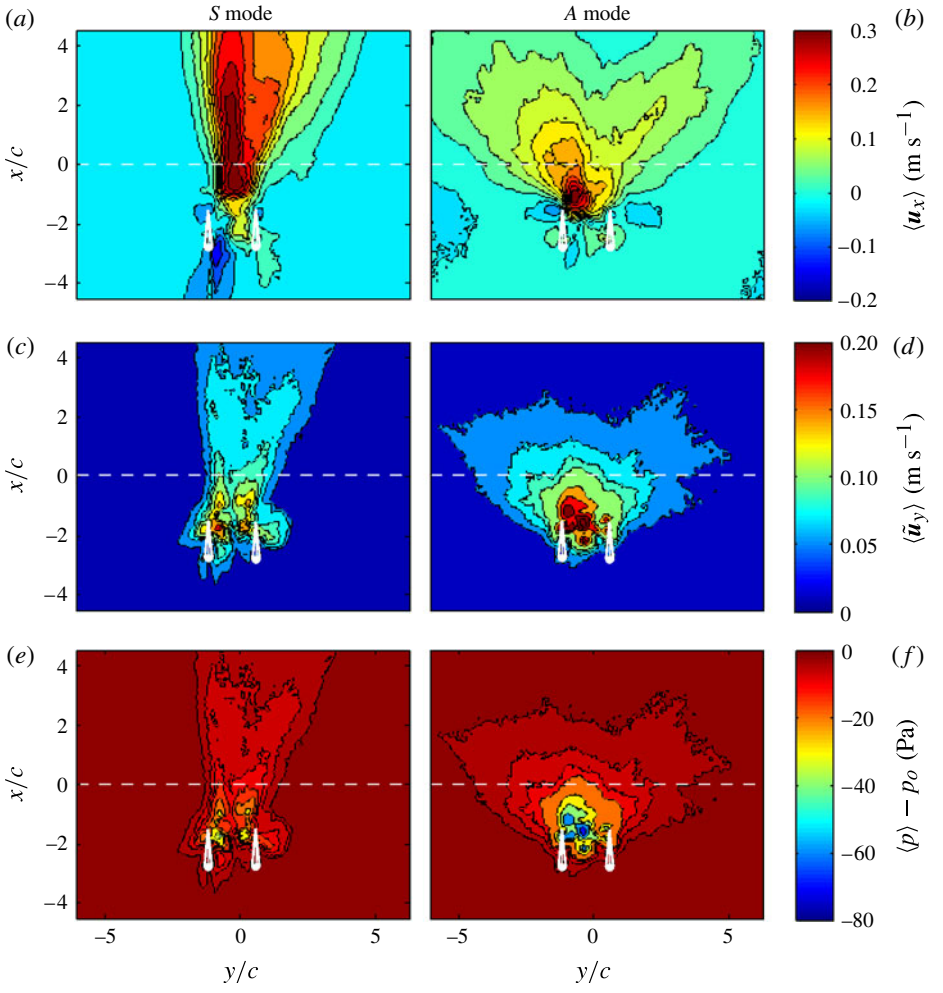

FIGURE 5. PIV measurements for $d/c = 1.47$ on both flapping configurations: (*a,b*) mean velocity measurements; (*c,d*) lateral fluctuations of the mean velocity; (*e,f*) pressure fields calculated from (3.4). The frequency was set to 5 Hz. Initial position of the flaps are schematized in white. Integrals were calculated over the white dashed line at $x/c = 0$ ($1.8c$ from the flaps' tip vertical position at $t = 0$).

Derivatives in (3.2) were calculated from PIV measurements to check the applicability of the turbulent boundary layer approximation to this case. In the free stream ($y \to \infty$) the pressure is p_o and $\langle \tilde{u}_y^2 \rangle$ is zero. The boundary conditions lead to

$$\langle p \rangle - p_o = -\rho \langle \tilde{u}_y^2 \rangle . \tag{3.4}$$

Equation (3.4) shows how the pressure in the wake is linked to the fluctuations of the transverse local velocity (see also the discussion in Raspa *et al.* (2012)). The $\langle \tilde{u}_y \rangle$ maps, extracted from the PIV measurements are displayed in figure 5(*c,d*) for both symmetric and asymmetric modes. The corresponding pressure, computed from (3.4), is presented in figure 5(*e,f*). Clearly, it can be seen that the asymmetric mode generates stronger fluctuations of the transversal velocity than its symmetric

counterpart and that, as a consequence, the near-wake pressure is significantly lower. Thus, the balance of (3.2) is changed through the second integral, modifying the amount of momentum available for propulsion (i.e. the force F_p). This interpretation is consistent with the fact that in the asymmetrical configuration, the lateral leaking of the momentum input applies lateral forces to the propeller (compensated by the physical constriction on the y-direction) that diminish the projection of the available force on the swimming direction respect to the symmetrical case where the leaking is minimized by the wake topology. At last, for each explored experimental condition, F_p can be evaluated through (3.2) from the corresponding velocity and pressure fields; and be compared with measurements obtained in the previous section. This is plotted in figure 4. Both quantities are very consistent in order of magnitude and general behaviour with respect to f, which validates PIV measurements to estimate the force in the two-dimensional approximation, but also strengthens the conjectures made on pressure in this paper.

4. Conclusions

We have shown that the way wakes are generated from the same momentum input has a noticeable effect on the swimming (or flying) performance of self-propelled objects. This dependence is mainly due to a pressure effect that is related to the intensity of the velocity fluctuations in the near wake. Although differences might be expected between the quasi-two-dimensional model wakes studied here and the real three-dimensional wakes encountered in nature, the effect of the spatial arrangement of the vortex shedding on the propulsive performance should prevail.

On the other hand, our measurements confirm that some wake configurations have the ability to minimize those fluctuations (here, for the symmetric mode for instance) and save useful momentum. The idea of flapping in a symmetrical configuration to get locomotive advantages in the context of fish schooling was reported by Childress (1981) and Kanso & Newton (2010). Animals are firstly constrained by their morphologies and needs, and some of them might spend more energy for the same work than others (Tytell 2007). However, one strategy of optimization for possible human made swimmers or flyers is therefore to control fluctuations in the wake by setting properly the time dependent momentum inputs to save energy. Further studies are currently being conducted in this way.

Acknowledgements

We thank all of the people at the PMMH workshop for their help with the experimental set-up. This work was supported by the French Research Agency (ANR-08-BLAN-0099) and by EADS Foundation through project ‘Fluids and elasticity in biomimetic propulsion’.

Supplementary material

Supplementary material are available at http://dx.doi.org/10.1017/jfm.2013.295.

REFERENCES

ANDERSON, E. J. & GROSENBAUGH, M. A. 2005 Jet flow in steadily swimming adult squid. *J. Expl Biol.* **208** (6), 1125–1146.

BATCHELOR, G. K. 1967 *An Introduction to Fluid Dynamics*. Cambridge University Press.

BIRCH, J. M., DICKSON, W. B. & DICKINSON, M. H. 2004 Force production and flow structure of the leading edge vortex on flapping wings at high and low Reynolds numbers. *J. Expl Biol.* **207** (7), 1063–1072.

BOHL, D. G. & KOOCHESFAHANI, M. M. 2009 MTV measurements of the vortical field in the wake of an aerofoil oscillating at high reduced frequency. *J. Fluid Mech.* **620**, 63–88.

CHILDRESS, S. 1981 *Mechanics of Swimming and Flying*. Cambridge University Press.

DABIRI, J. O., COLIN, S. P., COSTELLO, J. H. & GHARIB, M. 2005 Flow patterns generated by oblate medusan jellyfish: field measurements and laboratory analyses. *J. Expl Biol.* **208** (7), 1257–1265.

ELLINGTON, C. P., VAN DEN BERG, C., WILLMOTT, A. P. & THOMAS, A. L. R. 1996 Leading-edge vortices in insect flight. *Nature* **384**, 626–630.

FISH, F. E. & LAUDER, G. V. 2006 Passive and active flow control by swimming fishes and mammals. *Annu. Rev. Fluid Mech.* **38**, 193–224.

GODOY-DIANA, R., AIDER, J. L. & WESFREID, J. E. 2008 Transitions in the wake of a flapping foil. *Phys. Rev.* E **77**, 016308.

HEDENSTRÖM, A., ROSÉN, M. & SPEDDING, G. R. 2006 Vortex wakes generated by robins *Erithacus rubecula* during free flight in a wind tunnel. *J. Royal Soc. Interface* **3** (7), 263–276.

JOSLIN, R. D. 1998 Aircraft laminar flow control. *Annu. Rev. Fluid Mech.* **30** (1), 1–29.

KANSO, E. & NEWTON, P. K. 2010 Locomotory advantages to flapping out of phase. *Exp. Mechs.* **50**, 1367–1372.

KATZ, J. 2006 Aerodynamics of race cars. *Annu. Rev. Fluid Mech.* **38** (1), 27–63.

KRUEGER, P. 2005 An over-pressure correction to the slug model for vortex ring circulation. *J. Fluid Mech.* **545**, 427–443.

LIGHTHILL, M. J. 1960 Note on the swimming of slender fish.. *J. Fluid Mech.* **9**, 305–317.

MÜLLER, U., HEUVEL, B., STAMHUIS, E. & VIDELER, J. 1997 Fish foot prints: morphology and energetics of the wake behind a continuously swimming mullet (Chelon labrosus risso). *J. Expl Biol.* **200** (22), 2893–2906.

VAN OUDHEUSDEN, B. W., SCARANO, F., ROOSENBOOM, E. W. M., CASIMIRI, E. W. F. & SOUVEREIN, L. J. 2007 Evaluation of integral forces and pressure fields from planar velocimetry data for incompressible and compressible flows. *Exp. Fluids* **43** (2), 153–162.

PONCET, P. 2002 Vanishing of mode b in the wake behind a rotationally oscillating circular cylinder. *Phys. Fluids* **14**, 2021–2023.

POPE, S. B. 2000 *Turbulent Flows*. Cambridge University Press.

RAMANANARIVO, S., GODOY-DIANA, R. & THIRIA, B. 2011 Rather than resonance, flapping wing flyers may play on aerodynamics to improve performance. *Proc. Natl Acad. Sci. U.S.A.* **108**, 5964–5969.

RASPA, V., GAUBERT, C. & THIRIA, B. 2012 Manipulating thrust wakes: a parallel with biomimetic propulsion. *Europhys. Lett.* **97**, 44008.

RUIZ, L., WHITTLESEY, R. & DABIRI, J. 2011 Vortex-enhanced propulsion. *J. Fluid Mech.* **668**, 5–32.

SAFFMAN, P. G. 1992 *Vortex Dynamics*. Cambridge University Press.

SPALART, P. R. & MCLEAN, J. D. 2011 Drag reduction: enticing turbulence, and then an industry. *Phil. Trans. R. Soc.* A **369** (1940), 1556–1569.

SPEDDING, G. R. & HEDENSTRÖM, A. 2009 PIV-based investigations of animal flight. *Exp. Fluids* **46** (5), 749–763.

SUTHERLAND, K. R. & MADIN, L. P. 2010 Comparative jet wake structure and swimming performance of salps. *J. Expl Biol.* **213** (17), 2967–2975.

THIRIA, B., GOUJON-DURAND, S. & WESFREID, J. E. 2006 Wake of a cylinder performing rotary oscillations. *J. Fluid Mech.* **560**, 123–148.

TYTELL, E. D. 2007 Do trout swim better than eels? Challenges for estimating performance based on the wake of self-propelled bodies. *Exp. Fluids* **43** (5), 701–712.